


Cite this: *Mater. Adv.*, 2023,  
4, 157Received 4th October 2022,  
Accepted 4th November 2022

DOI: 10.1039/d2ma00951j

rsc.li/materials-advances

# Evidence of thermal ionization induced luminescence quenching in $\text{CePO}_4$ and $\text{GdPO}_4$ †

Suchinder K. Sharma 

The optical properties and their temperature dependence of two rare earth orthophosphates,  $\text{CePO}_4$  and  $\text{GdPO}_4$ , are presented.  $\text{CePO}_4$  shows prominent luminescence emission at wavelengths of 392 and 425 nm, typical of interconfigurational  $5d \rightarrow 4f$  transitions. For  $\text{GdPO}_4$ , the prominent emission is observed at a wavelength of 313 nm, due to intraconfigurational  $4f \rightarrow 4f$  transitions. Upon increasing the measurement temperature, the activation energy required to quench the luminescence emission is found to be 0.25 and 0.58 eV for  $\text{CePO}_4$  and  $\text{GdPO}_4$  samples, respectively.  $\text{GdPO}_4$  showed better thermal stability of the luminescence when compared to the  $\text{CePO}_4$  sample. Vacuum referred binding energy (VRBE) diagrams were prepared to determine the thermal quenching mechanisms in the two cases. It is observed that the quenching mechanism in both cases is dominated by thermal ionization of charges to the conduction band ( $\text{CePO}_4$ ) and the valence band ( $\text{GdPO}_4$ ). Thermoluminescence studies were performed to correlate the location of traps in the two samples and the corresponding thermal quenching mechanisms.

## 1 Introduction

The rare earth orthophosphates ( $\text{REPO}_4$ , RE = La to Lu) require lower annealing temperature when compared to other refractory oxides and are excellent optical materials possessing high brightness along with stable physical and chemical properties.<sup>1</sup> They also possess excellent thermal stability up to a temperature of 865 K, perfectly suitable for temperature sensing.<sup>2</sup> Among the two known structure-types of  $\text{REPO}_4$ , light-REs exhibit a monazite-type crystal structure (space group  $P2_1/n$ ), while heavy-REs have a xenotime-type crystal structure (space group  $P4_1/amd$ ). The rare earth ion Tb is an exception which can possess both crystal structure-types, monazite or xenotime. In our recent work on rare earth orthophosphates, we explored the temperature dependence of the optical properties of  $\text{EuPO}_4$  upon excitation with different wavelengths and established a new strategy to sense temperature.<sup>2</sup> The temperature dependence of the photoluminescence (PL) spectra of  $\text{SmPO}_4$  was also studied extensively to infer a non-quenching luminescence behaviour even up to very high temperatures.<sup>3</sup> The optical properties of single crystal samples of some other orthophosphates,  $\text{TbPO}_4$ ,  $\text{DyPO}_4$  and  $\text{PrPO}_4$ , exhibiting prominent emission in the green (545 nm), yellow (574 nm) and red (616 nm) regions of the electromagnetic spectrum, were also studied and

compared for their possible use in solid-state lighting devices.<sup>4</sup> In these studies, theoretical studies based on the chemical shift model [vacuum referred binding energy (VRBE) diagrams] were performed and combined with optical and thermally stimulated luminescence studies to understand the charge trapping–detrapping dynamics.

Within the same family of rare earth orthophosphates, two important members are cerium (Ce) and gadolinium (Gd) based  $\text{CePO}_4$  and  $\text{GdPO}_4$  orthophosphate samples. The Ce ion has 1 electron in the outermost shell which exhibits  $d \rightarrow f$  type characteristic luminescence emission, with the possibility to tune the emission from the UV to the red region, based upon the host crystal-field strength. On the other hand, Gd ions are known to produce deep-UV luminescence emission with the capability of exhibiting magnetic behaviour which can be used for magnetic resonance imaging (MRI) applications.<sup>5</sup> The presence of Gd is found to enhance the quality of MRI by altering the magnetic properties of water molecules within the body of the animal. By looking at the technological importance of Ce and Gd doped materials, and to extend our understanding of  $\text{REPO}_4$  hosts, the aim of the present work is to investigate single crystal samples of  $\text{CePO}_4$  and  $\text{GdPO}_4$ , the optical properties, and their temperature dependence in a wide temperature range of 293–873 K. The development of new, thermally stable inorganic materials requires a thorough understanding of the mechanisms responsible for thermal quenching in these materials. Cerium-containing materials exhibiting quenching of the  $5d \rightarrow 4f$  emission transitions is a result of one or a combination of the following three mechanisms: (a) non-radiative  $5d \rightarrow 4f$

Amity School of Physical Sciences, Amity University Punjab, IT City, Sector 82A, Mohali, 140308, India. E-mail: suchindersharma@gmail.com

† Electronic supplementary information (ESI) available: Fig. S1 and S2. See DOI: <https://doi.org/10.1039/d2ma00951j>

crossover relaxation *via* electron–phonon coupling, (b) thermal ionization of the 5d electron of cerium into the conduction band of the host lattice, followed by charge trapping at defects, and (c) thermally activated concentration quenching.<sup>6</sup> The mechanism in CePO<sub>4</sub> has not been explored so far and the mechanism in Gd doped materials is unclear and hence for both cases, detailed investigations are required. Based on these issues, another important objective of the present work is to understand the thermal quenching mechanisms in the two samples upon excitation into their absorption bands in the UV-region. It is observed that as soon as the sample temperature is increased above 450 K (for CePO<sub>4</sub>) and above 500 K (for GdPO<sub>4</sub>), the thermal quenching due to thermal ionization of charges is evident. The experimental observations were found to be in good agreement with the theoretical predictions performed for the two samples using VRBE diagrams suggesting that there is charge trapping and detrapping at the defects close to the conduction band and valence band for CePO<sub>4</sub> and GdPO<sub>4</sub> samples, respectively.

## 2 Experimental

### 2.1 Single crystal growth

The single crystal samples of CePO<sub>4</sub> and GdPO<sub>4</sub> were prepared by the flux technique in accordance with the synthesis procedure discussed in ref. 7 at the Oak Ridge National Laboratory, USA.<sup>8</sup> The samples are part of the Smithsonian standard samples generally used for electron microprobe analysis (EMPA). In a typical procedure, cerium and gadolinium oxide precursors are placed in a tightly covered platinum crucible containing PbHPO<sub>4</sub>, to form the flux matrix at high temperature and fired at 1633 K for 16 h. The crucibles were cooled to 1173 K and later quenched to room temperature (300 K). The crystals were then dissolved in HNO<sub>3</sub> to extract single crystal samples of CePO<sub>4</sub> and GdPO<sub>4</sub>.

### 2.2 Characterization

The high resolution colored two-dimensional images of the two single crystal samples were obtained on an Olympus LEXT OLS4000 confocal laser microscope with a 405 nm laser for surface profile analysis. The crystal structure was analyzed using VESTA software.<sup>12</sup> The diffuse reflectance spectra were obtained in the wavelength range of 190–1060 nm, at room temperature using a SPECORD S-600 UV/Vis spectrophotometer, procured from Analytik Jena AG, Germany. The room temperature photoluminescence (PL) spectra were measured after excitation using an EQ-99X LDLSTM laser-driven light source with a SG-600–500 hyperchromator from Mountain Photonics GmbH, Germany. The signals were detected using a liquid nitrogen cooled CCD camera (Princeton Instruments SPEC-10:100 BR eXcelon) coupled to an Acton SP2560i monochromator. The spectra were corrected for excitation source and detection optics. For the temperature dependent PL measurements, a Daybreak 1150 thermoluminescence (TL) reader was modified to simultaneously excite the sample, and record emission, in a temperature range of 293–865 K. The signal was

detected using a Newton 920 CCD camera from Andor Technology (Oxford Instruments), with Solis software for data acquisition. The CCD camera was attached to an Andor Shamrock SR163 Czerny–Turner spectrograph with a 300 g mm<sup>−1</sup> grating for the spectral resolution. The data was corrected for the blackbody radiation at high temperatures (> 653 K).

## 3 Results

### 3.1 Confocal microscopy and structure

The 2D images of the surface of the two single crystal samples in real-space and false-color height images are shown in Fig. 1(a and b). In the real-space images, the CePO<sub>4</sub> and GdPO<sub>4</sub> samples appear rigid with dimensions of  $\sim 750 \times 1200 \mu\text{m}$  and  $\sim 1700 \times 1800 \mu\text{m}$  (length  $\times$  width), respectively. The false color images evince different colors, green, blue and yellow, which could be due to different absorption/emission characteristics. The different heights in the false color images are encoded by different colors where the yellow color represents greater intensity (greater height) followed by green and blue colors having comparably lower height. Although, the growth of crystals is found to be uniform, *cf.* Fig. 1(a and b).

The structural parameters used in our present study have been reported in ref. 9 and 10 for CePO<sub>4</sub> and GdPO<sub>4</sub> samples, respectively. A comparison of the lattice parameters and axial ratio (*a/c*) is shown in Fig. 1(c). The real-time images for these two samples have also been reported in ref. 13. The lattice parameters decrease while the axial ratio (*a/c*) increases, as we increase the number of electrons from Ce to Gd. Both the samples possess a monazite-type crystal structure, Fig. 1(d). In the structure, the Ln atoms (Ce and Gd) are coordinated to nine oxygen atoms forming an REO<sub>9</sub> polyhedron, also described as a pentagonal interpenetrating tetrahedron. Such variation is due

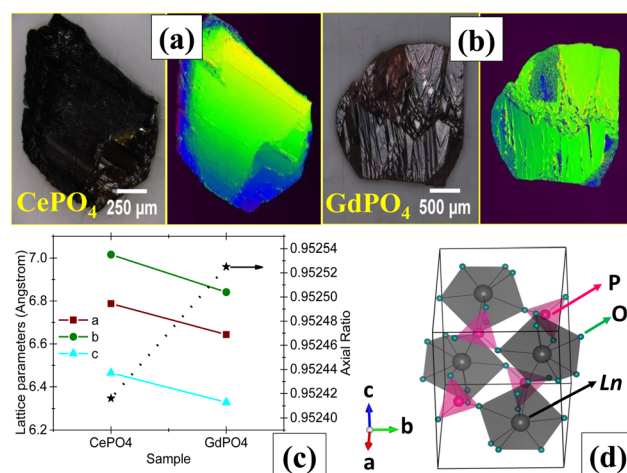


**Fig. 1** (a) Real space image (left) and false color height image (right) of the single crystal sample of CePO<sub>4</sub>; (b) real space image (left) and false color height image (right), to be considered relatively, of the single crystal sample of GdPO<sub>4</sub>; (c) variation of lattice parameters and axial ratio (*a/c*) for CePO<sub>4</sub> and GdPO<sub>4</sub> samples;<sup>9,10</sup> and (d) monazite-type crystal structure of LnPO<sub>4</sub> (Ln = Ce, Gd). The different heights in the false color images are encoded by different colors.



to a very slight distortion of the phosphate tetrahedron leading to bidentate bonding, resulting in a rigid structure where one corner of the adjacent  $\text{PO}_4$  tetrahedra rotates towards the RE ion, transforming  $\text{REO}_8$  into  $\text{REO}_9$  polyhedra, due to the larger ionic radius of La in comparison to Lu, which forms a xenotime-type crystal structure. The detailed lattice parameters for the two samples are shown in Table S1 (ESI†).

### 3.2 Luminescence studies at room temperature

**CePO<sub>4</sub>.** Two different studies, UV-Vis diffuse reflectance and luminescence emission spectroscopy, were carried out on both the samples at room temperature (RT). The diffuse reflectance spectrum for  $\text{CePO}_4$  is measured between the wavelengths of 190 and 450 nm, as shown in Fig. 2(a) (dark black line). In order to determine the bandgap and/or other higher absorption bands of  $\text{Ce}^{3+}$  in  $\text{CePO}_4$ , the excitation spectrum is also adopted from ref. 11, cf. Fig. 2(a) (royal blue line). No details of the diffuse reflectance spectra in the vacuum ultra-violet region could be found in the literature.  $\text{CePO}_4$  is an insulating material with a band gap of  $\sim 8.0$  eV, while the charge transfer band of Ce is observed at 7.00 eV.<sup>11</sup> Upon combining the two spectra in Fig. 2(a), four different absorption/excitation bands were observed (marked A, B, C, D) which overlap in the excitation and the absorption spectra. In the adopted excitation spectrum, additional bands at  $<185$  nm could also be seen. The four bands between A and D are assigned to  $\text{Ce}^{3+}$  inter-configurational  $4f \rightarrow 5d$  transitions as marked in Fig. 2(c). The host related band is observed at 150 nm (8.26 eV). The diffuse reflectance spectrum for our sample from a wavelength of 280 nm up to 350 nm could be related to the defects in the  $\text{CePO}_4$ . The other possibility of assigning this band to  $\text{O}^{2-} \rightarrow \text{Ce}^{4+}$  charge transfer can be ignored completely as such a band is expected around a wavelength of 180 nm.<sup>11</sup>

Hund described the fundamental state of  $\text{Ce}^{3+}$  to be  $^2F_{5/2}$  which was later proved and corrected by Lang using X-ray spectra, stating that the lowest Ce-4f state is a  $^2F_{5/2}$ - $^2F_{7/2}$  doublet separated from each other by  $2253 \pm 250 \text{ cm}^{-1}$  and  $50\,000 \text{ cm}^{-1}$  from the higher 5d level.<sup>14,15</sup> The emission spectrum of  $\text{CePO}_4$  upon excitation at a wavelength of 275 nm

exhibits two bands at 392 ( $25\,510 \text{ cm}^{-1}$ ) and 425 nm ( $23\,529 \text{ cm}^{-1}$ ) with a total separation of  $1980 \text{ cm}^{-1}$ . The value is in good agreement with the expected separation between  $^2F_{5/2}$  and  $^2F_{7/2}$ ,<sup>15</sup> suggesting that these two emissions originate purely from  $\text{Ce}^{3+} 5d \rightarrow 4f [^2F_{(5/2),(7/2)}]$  transitions. The respective absorption and emission transitions are compared for a  $\text{Ce}^{3+}$  ion in a vacuum and in the  $\text{CePO}_4$  host using an energy level diagram as shown in Fig. 2(c). The absorption/excitation is typically due to interconfigurational  $4f \rightarrow 5d$  transitions (upward arrows), while the emission is due to  $5d_1 \rightarrow 4f$  transitions (downward arrows), respectively.

**GdPO<sub>4</sub>.** The diffuse reflectance spectrum of  $\text{GdPO}_4$  is shown in Fig. 3(a). The spectrum from ref. 11 is considered to compare and extend the reflectance spectrum to cover band gap excitation. However, as the adopted data does not present absolute diffuse reflectance, two different y-scales are used to collate the two spectra, cf. Fig. 3(a). The spectrum from the adopted work, and our measured spectrum overlap for absorption at a wavelength of 285 nm, marked A in Fig. 3(a). For our measurements, another absorption band is observed at 310 nm (marked B). The two absorption transitions are shown in a  $\text{Gd}^{3+}$  energy level diagram, Fig. 3(c) (upward arrows). A more detailed investigation on the change in absorption bandgaps among different rare earth orthophosphates is presented in ref. 16.

The  $\text{Gd}^{3+}$  luminescence emission spectrum is shown in Fig. 3(b). The emission spectrum is located in the UV-region of the electromagnetic spectrum with a maximum at 313 nm along with some other lines at wavelengths of 323 and 326 nm. These higher wavelength transitions are assigned to the weak vibronic transitions of  $\text{Gd}^{3+}$  and are in accordance with the expected value of  $\sim 1350 \text{ cm}^{-1}$  below the prominent emission at 313 nm.<sup>17</sup> The main transition at a wavelength of 313 nm can be assigned to the  $^6P_{7/2} \rightarrow ^8S_{7/2}$  electronic transition. Moreover, we also observe small kinks in the emission spectrum for the main transition at 313 nm, cf. Fig. 3(b). These can be assigned to the higher crystal field levels of the  $^6P_{7/2}$  level. Since the crystal field for lanthanides with f-f type transitions is expected to be small, measurements at helium temperature are required to provide detailed investigations on the influence of crystal

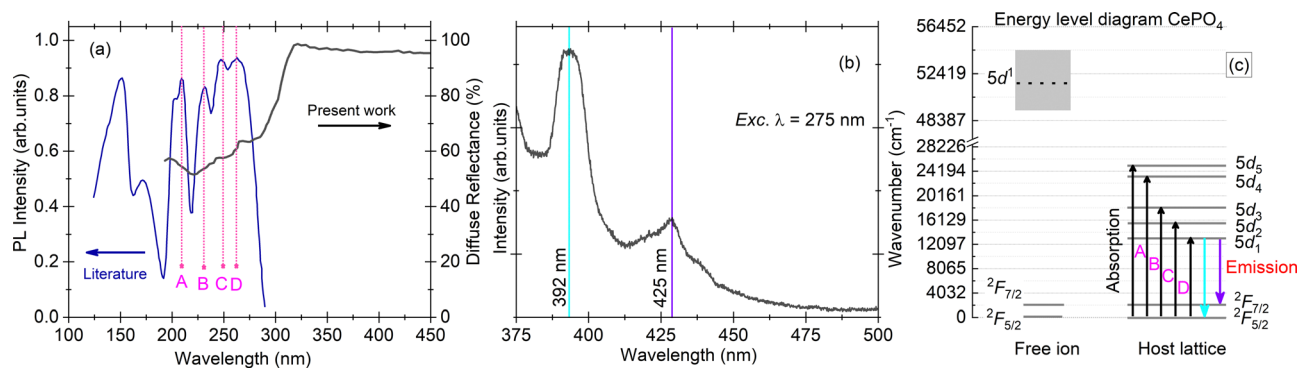


**Fig. 2** (a) Diffuse reflectance spectrum for a single crystal sample of  $\text{CePO}_4$  (present work, dark black line) and excitation spectrum for the same sample from the literature (royal blue line),<sup>11</sup> along with marked positions of the  $\text{Ce}^{3+} 4f \rightarrow 5d$  transitions (A–D); (b) PL emission spectrum with maxima at 392 and 425 nm, measured for excitation at a wavelength of 275 nm; and (c) energy level diagram of the  $\text{Ce}^{3+}$  ion in a vacuum and in the  $\text{CePO}_4$  host. All the measurements were performed at room temperature.

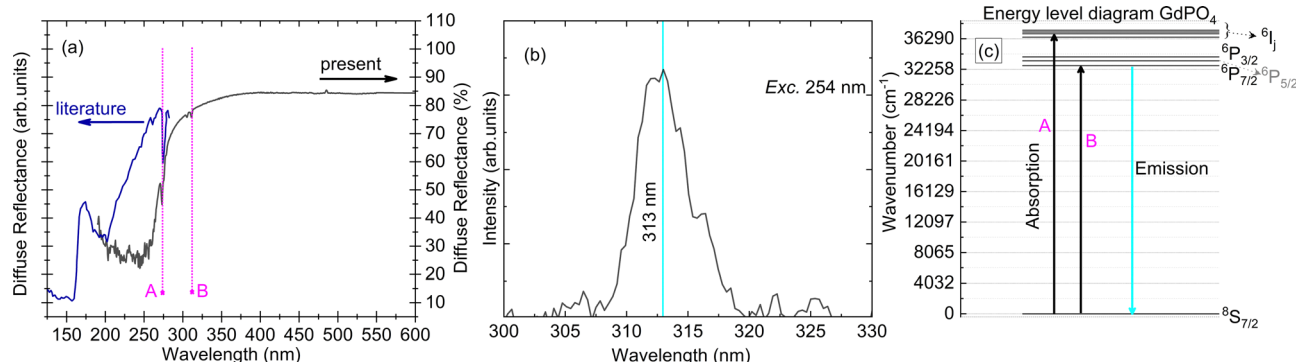


Fig. 3 (a) Diffuse reflectance spectrum for a single crystal sample of  $\text{GdPO}_4$  (present work, dark black line) and from the literature (royal blue line),<sup>11</sup> along with marked positions of the  $\text{Gd}^{3+}$  4f–4f transitions (A and B); (b) PL emission spectrum with maxima at 313 nm, measured for excitation at a wavelength of 254 nm; and (c) energy level diagram of the  $\text{Gd}^{3+}$  ion in a vacuum along with marked transitions for absorption and emission. All the measurements were performed at room temperature.

field on  $^6\text{P}_{7/2}$  multiplets, which paves the way for further research. Usually, one can expect four different crystal-field levels of  $^6\text{P}_J$  upon excitation with UV, and other  $^6\text{P}$ ,  $^6\text{I}$ ,  $^6\text{D}$  and  $^6\text{G}$  level related emission upon excitation with higher energy, for example, when excited with X-rays.<sup>18</sup>

The energy level scheme of the  $\text{Gd}^{3+}$  ion was first discussed by Piksis<sup>19</sup> for energy up to  $40\,590\text{ cm}^{-1}$ , and later by Wegh<sup>20</sup> in the vacuum ultraviolet energy region ( $50\,000\text{--}70\,000\text{ cm}^{-1}$ ). The  $\text{Gd}^{3+}$  ion has a half-filled configuration,  $[\text{Xe}]4f^75s^25p^6$ , which gives a stable  $^8\text{S}_{7/2}$  ground state. The  $^8\text{S}_{7/2}$  state is orbitally non-degenerate and cannot be split by the crystal field resulting in a single line. The excited state of  $\text{Gd}^{3+}$  has two set of multiplets corresponding to  $^6\text{P}_J$  and  $^6\text{I}_J$  in the UV-region ( $J$  is the quantum number for total angular momentum), along with other higher energy multiplets due to  $^6\text{D}_J$  in the vacuum ultra-violet region [the ones corresponding to  $^6\text{P}_J$  and  $^6\text{I}_J$  are shown in Fig. 3(c)]. Because the  $4f^7$  shell is shielded by  $5s^2$  and  $5p^6$  electrons, the position and order of  $^6\text{P}_J$ ,  $^6\text{I}_J$  and  $^6\text{D}_J$  are almost independent of host choice. The diffuse reflectance spectra in Fig. 3(a) show two absorption lines (marked A and B) which correspond to transitions from the ground state,  $^8\text{S}_{7/2}$  to higher  $^6\text{P}_J$  and  $^6\text{I}_J$  states, respectively, in increasing order of energy. The Stark components of these transitions (in absorption and emission) could not be resolved further due to experimental limitations. The band gap of the material is 7.8 eV as determined in an earlier report.<sup>11</sup>

### 3.3 Luminescence studies at high temperature

**CePO<sub>4</sub>.** The temperature dependence of the photoluminescence (PL) emission is studied at high temperature between 293 and 873 K, Fig. 4(a). The spectra were obtained for excitation at a wavelength of 254 nm. The emission spectrum under 254 nm excitation shows two prominent emission bands at wavelengths of 392 and 453 nm, for measurement at a temperature of 293 K. Similar values are reported in ref. 21. As the temperature is increased, two important observations regarding PL emission were: (a) a decrease in the PL emission intensity is noticeable for all the increased temperatures between 293 and 873 K; and (b) the emission spectrum shifts – 392 to 384 nm and 453 to

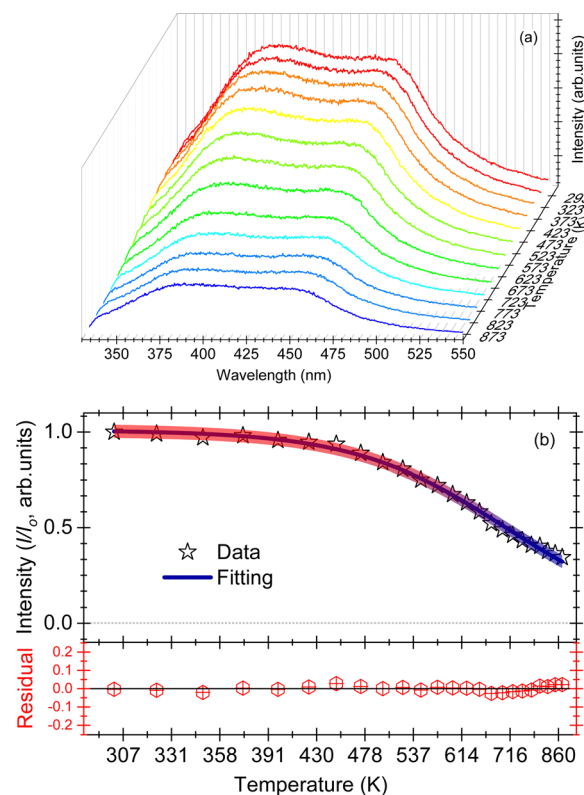


Fig. 4 (a) Waterfall plots of PL intensity of  $\text{CePO}_4$  between temperatures of 293 and 873 K, for excitation at a wavelength of 254 nm; (b) integrated PL emission intensity between wavelengths of 360 and 550 nm, as a function of increasing temperature. The residual obtained after subtracting the fitted data from the experimental data is also shown for a comparison.

443 nm for measurement at the lowest and highest temperature, 293 and 873 K, respectively. The separation between 392 and 453 nm is found to be  $\sim 3400\text{ cm}^{-1}$  which is slightly higher than the expected value of  $2250\text{ cm}^{-1}$ . This could be due to the change in the excitation wavelengths, for example resonant [275 nm in Fig. 2(b)] and non-resonant excitation [254 nm in the present case], used to obtain the two luminescence spectra.



The emission spectrum is a culmination of two bands where the probability of transition from one decreases and the probability of transition for another increases when we change the excitation wavelength along with increasing the temperature. Due to this change in transition probability, the relative ratio of the two bands changes and a shift in the emission maxima is observed.

The effect of temperature on the thermal quenching of  $\text{CePO}_4$  is determined by normalizing the high temperature luminescence curves up to 873 K with respect to the emission spectrum measured at 273 K. The onset of the quenching temperature ( $T_{95\%}$ ) and the thermal quenching temperature ( $T_{50\%}$ ) can be defined as the temperatures at which the emission intensity decreases to 95% and 50% of the initial emission intensity at room temperature, respectively. For  $\text{CePO}_4$ ,  $T_{95\%}$  is evaluated to be a temperature of 430 K, while  $T_{50\%}$  is found to be a temperature of 640 K, cf. Fig. 4(b). The sample showed lower stability of the PL in comparison to  $\text{TbPO}_4$  ( $T_{50\%} = 730$  K), and better thermal stability than  $\text{PrPO}_4$  ( $T_{50\%} = 540$  K) and  $\text{DyPO}_4$  ( $T_{50\%} = 490$  K). Although, in all the above cases, different excitation wavelengths can also lead to a change in the  $T_{50\%}$  temperature. To determine the activation energy, a single barrier quenching model was used to fit the thermal quenching curve in Fig. 4(b) using eqn (1):<sup>22</sup>

$$I(T) = \frac{I_0}{1 + \frac{\Gamma_n}{\Gamma_r} \exp(-E_a/k_B T)} \quad (1)$$

where  $I(T)$  is the intensity at temperature  $T$ ,  $I_0$  is the initial intensity at room temperature,  $\Gamma_r$  is the radiative recombination rate,  $\Gamma_n$  is the non-radiative recombination rate,  $E_a$  is the activation energy, and  $k_B$  is the Boltzmann constant. Upon fitting, the activation energy  $E_a$  is calculated to be  $0.25 \pm 0.01$  eV. The residual for the fitted thermal quenching curve (experimental data – fitted data) is also shown in Fig. 4(b), for comparison. A good agreement between the experimental curve and the fitted curve is obtained.

**GdPO<sub>4</sub>.** The temperature dependence of the emission spectra for the  $\text{GdPO}_4$  sample is also measured in the temperature region of 293–873 K, as shown in Fig. 5(a). The prominent emission is observed at 313 nm at a temperature of 293 K, similar to that observed with a different setup, Fig. 3(b). We anticipate two possible reasons for this: (a) the excitation wavelength was the same in both cases, and (b) the excitation/emission transitions in  $\text{Gd}^{3+}$  are of intraconfigurational f–f type which are less affected by the choice of excitation wavelength and the choice of host lattice due to the shielding effect. As the temperature is increased above 293 K, no shift in the emission spectra could be seen, instead a decrease in the emission intensity is observed. The change in the emission intensity with temperature is also known as thermal quenching of the optical material which was explored further.

The thermal quenching curve for the sample  $\text{GdPO}_4$  is shown in Fig. 5(b). The onset of the quenching ( $T_{95\%}$ ) and the thermal quenching temperature ( $T_{50\%}$ ) for the  $\text{GdPO}_4$  sample are evaluated to be 510 and 665 K, respectively [cf. Fig. 5(b)].

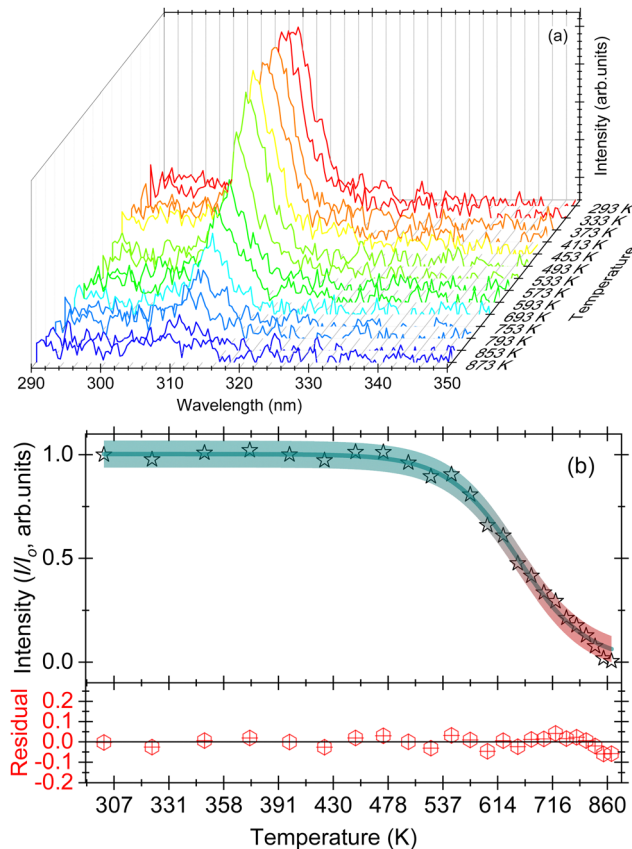


Fig. 5 (a) Waterfall plots of PL intensity of  $\text{GdPO}_4$  between temperatures of 293 and 873 K, for excitation at a wavelength of 254 nm; (b) integrated PL emission intensity between 300 and 320 nm as a function of increasing temperature. The residual obtained after subtracting the fitted data from the experimental data is also shown for a comparison.

We used eqn (1) to fit the thermal quenching curve as shown in Fig. 5(b) where the residual (experimental – fitted data) is also shown. The activation energy upon fitting the data is calculated at  $0.58 \pm 0.03$  eV having a good agreement between the experimental data and the fitted data.

### 3.4 Thermoluminescence

The thermoluminescence (TL) glow curves for the two samples under a  $\beta$ -dose fluence of 20 Gy are shown in Fig. 6. The glow curve for  $\text{CePO}_4$  shows a maximum at 365 K with approximate trap depth (activation energy,  $E_a$ ) of 0.78 eV calculated using a first order kinetic equation,  $25k_B T_m$ ,<sup>23</sup> where  $k_B$  is Boltzmann's constant and  $T_m$  is the glow curve maximum. The glow curve maximum at 365 K is similar to that observed for  $\text{DyPO}_4$ ,<sup>4</sup>  $\text{SmPO}_4$  and  $\text{EuPO}_4$  samples,<sup>3</sup> suggesting that the origin of this glow curve maximum is an intrinsic defect which is formed due to the host lattice and is independent of the choice of the rare earth ion. This defect has similar trap depth in all the samples. The high temperature increase in the TL signal for temperature  $> 560$  K in the  $\text{CePO}_4$  sample is related to the black body radiation from the stainless steel disc used for placing the sample inside a TL reader. The glow curve for  $\text{GdPO}_4$  possesses three maxima at 365, 500 and 590 K, with  $E_a = 0.78$ , 1.02 and



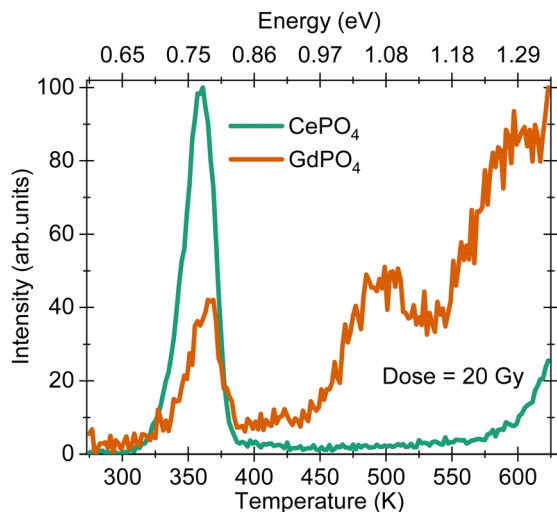


Fig. 6 Thermoluminescence glow curves of  $\text{CePO}_4$  and  $\text{GdPO}_4$  samples recorded upon exposure to a 20 Gy  $\beta$ -dose. The glow curves were recorded with a heating rate of  $2 \text{ K s}^{-1}$  without using any filter in the detection path.

1.30 eV, respectively [cf. Fig. 6]. The glow peak maximum at 365 K is similar to that observed for the  $\text{CePO}_4$  sample.

## 4 Discussion

$\text{CePO}_4$  and  $\text{GdPO}_4$  are two interesting and important members of the rare earth orthophosphate family. For  $\text{CePO}_4$ , the  $\text{Ce}^{3+}$  ion acts as a luminescent center with prominent emission at 392 and 425 nm due to electric- and spin-allowed dipole transitions from the 5d state to the multiplets of the fundamental 4f configuration. Depending upon the site symmetry, the five most distinct 4f–5d transitions can be observed in the absorption spectra of  $\text{Ce}^{3+}$ . Since the electron–phonon coupling spectra of the 4f and 5d electrons are different in  $\text{Ce}^{3+}$ , the parity allowed electron–dipole transitions between the 4f and 5d states exhibit broad absorption and emission bands and the average position of the 5d bands decreases when compared to the position of free ions, which is also called centroid or barycentre shift.<sup>24</sup> The energy of the radiative transitions depends on the energy of the 5d component in the crystal field and also its degree of coupling with the lattice phonons. Fig. 7 compares the emission transitions of  $\text{Ce}^{3+}$  in different rare earth orthophosphate hosts,  $\text{YPO}_4$ ,  $\text{LaPO}_4$ ,  $\text{CePO}_4$ , and  $\text{LuPO}_4$ . While  $\text{LaPO}_4$  and  $\text{CePO}_4$  possess a monazite-type crystal structure, the  $\text{YPO}_4$  and  $\text{LuPO}_4$  hosts have a xenotime-type crystal structure. The impact of crystal structure is found to influence the crystal field of  $\text{Ce}^{3+}$  ions in these hosts. As we move from La to Ce based rare earth orthophosphates, the crystal field decreases thus increasing the overall separation between the lowest of the 5d<sub>1</sub> and 4f levels. The decrease in crystal field is in direct correlation with the lanthanide contraction effect where the ionic and atomic radii decrease with an increase in the atomic number.<sup>13</sup> For the xenotime type structure, the influence/crystal field is found to be higher when compared to the orthophosphates with monazite-type structure.

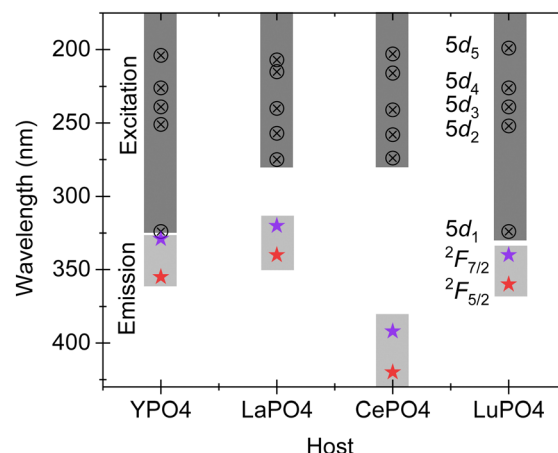


Fig. 7 Comparison of five different  $\text{Ce}^{3+}$  related absorption bands and emission bands among different hosts;  $\text{YPO}_4$  and  $\text{LuPO}_4$  possess a xenotime-type crystal structure while  $\text{LaPO}_4$  and  $\text{CePO}_4$  have a monazite-type crystal structure.

This implies that the separation between the lowest 5d<sub>1</sub> and 4f levels is the lowest with a prominent emission around a wavelength of 340 nm. For  $\text{LaPO}_4$ , the prominent emission is observed in the UV-region at a wavelength of 320–340 nm, while the prominent emission in the case of  $\text{CePO}_4$  is observed at 392 and 425 nm. Overall, the band gap of  $\text{CePO}_4$  is 8.0 eV upon combining diffuse reflectance spectra from the present and the earlier work, and the crystal field effect is much greater in rare earth orthophosphates with a xenotime-type crystal structure when compared with rare earth orthophosphates exhibiting a monazite-type crystal structure.

However, when  $\text{Gd}^{3+}$  is present as a luminescence center in samples with a monazite-type crystal structure, for example  $\text{LaPO}_4$ ,<sup>25</sup> and  $\text{GdPO}_4$  (the present work), or in  $\text{YPO}_4$ <sup>26</sup> with a xenotime-type structure, the emission maximum is consistent at  $312 \pm 1 \text{ nm}$  suggesting that the crystal field has negligible or no effect despite their comparatively different crystal structures. This clearly suggests that there is shielding of  $\text{Gd}^{3+}$  4f levels both in the ground as well as the excited states.

Finally, to understand the causes of variation in thermal quenching temperature and activation energy ( $E_a$ ), we prepared vacuum referred binding energy (VRBE) diagrams for  $\text{LaPO}_4$  and  $\text{GdPO}_4$ , Fig. S1 and S2 (ESI<sup>†</sup>), respectively. The data used to construct the VRBE diagram has been published by Dorenbos.<sup>27</sup> In  $\text{LaPO}_4$ ,  $\text{Ce}^{3+}$  is located  $\sim 0.25 \text{ eV}$  below the conduction band edge, Fig. S1 (ESI<sup>†</sup>). This value is in good agreement with the  $E_a$  value calculated from the thermal quenching curve, cf. Fig. 4(b). This  $E_a$  (0.25 eV) when translated to the TL glow curve, should show up at  $\sim 115 \text{ K}$  on the temperature vs. intensity scale (TL curve). This temperature is much lower than the current temperature range, 273–873 K, used to record TL glow curves. For  $\text{GdPO}_4$ , the  $E_a$  evaluated from the thermal quenching curves is  $0.58 \pm 0.03 \text{ eV}$ , cf. Fig. 5(b). When we compare this value with the separation between the conduction band edge and the highest 4f state of  $\text{Gd}^{3+}$  ions, a value of 1.29 eV is expected. This value is also observed in the TL glow curve for the  $\text{GdPO}_4$  sample where a



glow curve maximum is observed at 1.30 eV along with other maxima at 0.78 and 1.02 eV, cf. Fig. 6. The trap with trap depth 1.30 eV matches closely with the predicted value of 1.29 eV from the VRBE diagram suggesting that this defect acts as an electron trap. The nature of other defects at 1.02 eV could not be determined although based on the earlier observations, the trap with trap depth 0.78 eV is anticipated to belong to the intrinsic defect corresponding to the release of a hole from an unidentified host associated hole trap.<sup>16</sup> There can be two different ways to understand the luminescence quenching mechanisms in rare earth doped hosts: (a) *via* electron ionisation to the conduction band, and (b) *via* hole ionisation to the valence band. The  $E_a = 0.58$  eV for GdPO<sub>4</sub> matches closely with the 0.78 eV value (host associated hole trap). Hence, the thermal quenching in GdPO<sub>4</sub> is due to the thermal ionization of holes close to the valence band, while for the CePO<sub>4</sub> sample, thermal ionization of electrons close to the conduction band dominates. The  $E_a = 0.58$  eV for GdPO<sub>4</sub> is also found to be higher than that of the CePO<sub>4</sub> sample which suggests that the GdPO<sub>4</sub> sample has higher thermal stability and can act as a better charge reservoir than the CePO<sub>4</sub> sample.

## 5 Conclusions

The present work investigates, in detail, the optical properties of single crystal samples of CePO<sub>4</sub> and GdPO<sub>4</sub>, under UV excitation for possible use as charge reservoirs. CePO<sub>4</sub> shows double band emission spectra with maxima at wavelengths of 392 and 425 nm, with a separation of about 1980 cm<sup>-1</sup> which corresponds to Ce<sup>3+</sup> 5d → 4f interconfigurational transitions. The emission in GdPO<sub>4</sub> is typical of intraconfigurational f-f type with prominent UVB emission at a wavelength of 313 nm. The CePO<sub>4</sub> and GdPO<sub>4</sub> samples possess different thermal quenching temperatures, 640 and 665 K, with GdPO<sub>4</sub> exhibiting better thermal stability for charge storage applications. The activation energy in the two cases is found to be 0.25 and 0.58 eV for CePO<sub>4</sub> and GdPO<sub>4</sub> samples, respectively. The values are in good agreement with the theoretical calculations performed using the chemical shift model (VRBE diagrams), suggesting that the thermal quenching in CePO<sub>4</sub> is dominated by thermal ionization of charges to the conduction band. In the case of GdPO<sub>4</sub> the thermal quenching is dominated by thermal ionization of charges to the valence band, suggesting that the thermal quenching phenomenon in both cases is dominated by the thermal ionization mechanism.

## Conflicts of interest

There are no conflicts to declare.

## Acknowledgements

The author thanks Prof. Johannes Heitmann and Dr Jan Beyer of the Institute of Applied Physics, TU Bergakademie Freiberg, Germany for providing experimental facilities and their input on the draft of the manuscript. The author also thanks Prof. Richard Gloaguen and Dr Margret Fuchs of Helmholtz-Institute

Freiberg for Resource Technology, Freiberg-Germany, and the Department of Mineral Sciences of the Smithsonian Institution, for providing the reference samples [Catalog # NMNH 168484 (CePO<sub>4</sub>) and NMNH 168488 (GdPO<sub>4</sub>)]. The author thanks Thomas Behm for measurement support with the confocal microscope, and Thomas Köhler for support with UV-Vis diffuse reflectance spectra of both the samples.

## Notes and references

- 1 S. Achary, S. Bevara and A. Tyagi, *Coord. Chem. Rev.*, 2017, **340**, 266–297.
- 2 S. K. Sharma, T. Kohler, J. Beyer, M. Fuchs, R. Gloaguen and J. Heitmann, *Phys. Chem. Chem. Phys.*, 2019, **21**, 16329–16336.
- 3 S. K. Sharma, J. Beyer, R. Gloaguen and J. Heitmann, *Phys. Chem. Chem. Phys.*, 2019, **21**, 25669–25677.
- 4 S. K. Sharma, J. Beyer, R. Gloaguen and J. Heitmann, *Phys. Chem. Chem. Phys.*, 2020, **22**, 10247–10255.
- 5 C. Richard, B.-T. Doan, J.-C. Beloeil, M. Bessodes, V. Tóth and D. Scherman, *Nano Lett.*, 2008, **8**, 232–236.
- 6 Y.-C. Lin, M. Bettinelli and M. Karlsson, *Chem. Mater.*, 2019, **31**, 3851–3862.
- 7 R. S. Feigelson, *J. Am. Ceram. Soc.*, 1964, **47**, 257–258.
- 8 E. Jarosewich and L. A. Boatner, *Geostand. Newsl.*, 1991, **15**, 397–399.
- 9 G. Beall, L. Boatner, D. Mullica and W. Milligan, *J. Inorg. Nucl. Chem.*, 1981, **43**, 101–105.
- 10 D. F. Mullica, D. A. Grossie and L. A. Boatner, *Inorg. Chim. Acta*, 1985, **109**, 105–110.
- 11 A. Mayolet, PhD thesis, Institut de Physique Nucleaire, Universite Paris - SUD, Orsay, France, 1995.
- 12 K. Momma and F. Izumi, *J. Appl. Crystallogr.*, 2011, **44**, 1272–1276.
- 13 S. K. Sharma, T. Behm, T. Köhler, J. Beyer, R. Gloaguen and J. Heitmann, *Crystals*, 2020, **10**(7), 593.
- 14 F. Hund, *Z. Phys.*, 1925, **33**, 855–859.
- 15 R. J. Lang, *Can. J. Res.*, 1936, **14a**, 127–130.
- 16 T. Lyu and P. Dorenbos, *J. Mater. Chem. C*, 2018, **6**, 369–379.
- 17 G. Blasse, *Int. Rev. Phys. Chem.*, 1992, **11**, 71–100.
- 18 G. L. H. Brixner, *Chem. Phys. Lett.*, 1989, **157**, 283–288.
- 19 A. H. Piskis, G. H. Dieke and H. M. Crosswhite, *J. Chem. Phys.*, 1967, **47**, 5083–5089.
- 20 R. T. Wegh, H. Donker, A. Meijerink, R. J. Lamminmäki and J. Hölsä, *Phys. Rev. B: Condens. Matter Mater. Phys.*, 1997, **56**, 13841–13848.
- 21 N. Ekthammathat, T. Thongtem, A. Phuruangrat and S. Thongtem, *J. Nanomater.*, 2012, **2012**, 958593.
- 22 C. W. Struck and W. H. Fonger, *J. Lumin.*, 1975, **10**, 1–30.
- 23 C. Furetta, *Handbook of thermoluminescence*, World Scientific Pub., 2003, p. 461.
- 24 S. K. Sharma, *Phosphors: Synthesis and Applications*, 2018, 49.
- 25 A. Chauhan, A. Gawande and S. Omanwar, *Optik*, 2016, **127**, 6647–6652.
- 26 V. Singh, A. Prasad, A. Rao, S. W. Jung, N. Singh and M. Irfan, *Optik*, 2021, **225**, 165804.
- 27 P. Dorenbos, *J. Phys.: Condens. Matter*, 2013, **25**, 225501.

